Article

Enhanced Photo-Fenton Degradation of Antibiotics through Internal Electric Field Formation at the Interface of Mixed-Phase FeS_2

Hongyan Liu [1,2], Yunhang Shao [1,2], Shuai Dou [1,2] and Chengsi Pan [1,2,*]

[1] Key Laboratory of Synthetic and Biological Colloids, Ministry of Education, School of Chemical and Material Engineering, Jiangnan University, Wuxi 214122, China
[2] International Joint Research Center for Photoresponsive Molecules and Materials, Jiangnan University, Wuxi 214122, China
* Correspondence: cspan@jiangnan.edu.cn
Received: 9 September 2024; Revised: 9 October 2024; Accepted: 13 November 2024; Published: 15 November 2024

Abstract: Iron sulfide (FeS_2) is a rich mineral resource widely used as an efficient Fenton and photo-Fenton reagent due to its non-toxicity and low synthesis cost. However, the mechanism underlying its photo-Fenton degradation activity related to the two crystal phases—pyrite (P-FeS_2) and marcasite (M-FeS_2)—is still not well understood. In this study, P-FeS_2, M-FeS_2, and their mixed phase (P/M-FeS_2) were prepared through hydrothermal reactions. The results showed that P/M-FeS_2 exhibited the highest photo-Fenton degradation activity, achieving a removal rate of approximately 99% for 50 ppm of ciprofloxacin (CIP) within 3 minutes, outperforming other photo-Fenton catalysts in pollutant degradation. The study revealed that an internal electric field (IEF) is generated at the interface of M-FeS_2 and P-FeS_2 due to their differing work functions. This IEF accelerates the regeneration of the active sites (Fe^{2+} in S_2^{2-}-P-FeS_2 and M-FeS_2) required for the Fenton reaction, thereby explaining the superior activity of the P/M-FeS_2 mixed phase. This study introduces the IEF theory for the first time to explain the mechanism of mixed-phase catalysts in the photo-Fenton reaction. The formation of IEF can enhance the regeneration of the active sites involved in the Fenton reaction, thereby improving both reaction activity and stability. This work highlights the significance of regulating crystal phases in the degradation of pollutants during heterogeneous Fenton reactions and offers insights for developing highly efficient Fenton catalysts.

Keywords: Fenton; FeS_2; crystal phases; antibiotics; internal electric field

1. Introduction

Ciprofloxacin (CIP) is widely prescribed as a third-generation fluoroquinolone antibiotic for treating various bacterial infections [1]. Recently, concerns have arisen regarding its residual wastewater's adverse effects on human health and its harmful impact on aquatic ecosystems [2–4]. Due to its large molecular size, complex structure, and potent antimicrobial properties, ciprofloxacin is resistant to degradation by natural microorganisms [5]. Conventional water treatment plants typically employ methods like adsorption, flocculation precipitation, and biodegradation, but these methods often struggle to effectively eliminate antibiotics [6,7]. For instance, conventional biological methods require more than 10 days to remove 2 ppm of ciprofloxacin from the water environment [8]. Addressing antibiotic residue degradation is critical for achieving sustainable development and environmental management goals.

The Fenton process represents an advanced oxidation technology that generates hydroxyl radicals with a high oxidation potential (2.8 eV) through the reaction of Fe^{2+} with hydrogen peroxide [9]. These radicals effectively mineralize nearly all types of organic pollutants into CO_2 and H_2O [10]. However, Fenton systems suffer from inefficient Fe^{2+}/Fe^{3+} cycling, leading to the yield of Fe sludge and limiting their overall degradation efficiency [11]. The photo-Fenton catalytic technology is developed to boost the oxidation efficiency of the Fenton reaction, integrating the benefits of both photochemical reactions and the Fenton reaction [12]. In photochemical reactions, the reduction rate of iron (III) is enhanced under light conditions because of the improved photoinduced oxidation of iron (III) or the ligands of the iron (III) complex with organic pollutants, or their degradation intermediates [13]. This further increases the production of hydroxyl radicals (•OH), thereby improving the degradation rate and overall pollutant removal efficiency.

Copyright: © 2024 by the authors. This is an open access article under the terms and conditions of the Creative Commons Attribution (CC BY) license (https://creativecommons.org/licenses/by/4.0/).
Publisher's Note: Scilight stays neutral with regard to jurisdictional claims in published maps and institutional affiliations

The heterogeneous photo-Fenton system, in particular, has gained increasing attention because it addresses some of the limitations of the homogeneous photo-Fenton process, such as stringent pH requirements, the formation of iron sludge, and challenges related to catalyst recovery. However, these catalysts still face challenges such as low efficiency and slow reaction rates, relative to the homogeneous photo-Fenton systems. For instance, according to the literature, when the heterogeneous catalyst α-Fe_2O_3 is employed for mineralizing 10 ppm CIP, the removal percentage of CIP at 180 min is only 58.8% [14]. This efficiency is significantly lower compared to that achieved by homogeneous catalysts. Thus, developing heterogeneous catalysts with high degradation rates has become a focal point in enhancing the efficiency of Fenton reactions for pollutant degradation.

Iron-based catalysts like Fe_3O_4 and Fe_2O_3 are known for their efficacy in heterogeneous photo-Fenton degradation [15,16]. Among these iron salts, FeS_2 is the most abundant mineral on the Earth's surface and offers superior catalytic efficiency at a significantly lower cost [17]. Recently, FeS_2 has emerged as an effective Fenton reagent to remove organic pollutants [18]. For example, Yang et al. demonstrated that pyrite efficiently degraded 50 ppm p-nitrophenol in 4 min with H_2O_2 addition and light irradiation [19]. For another example, Xue et al. found that 50 ppm methylene blue is degraded in 30 min in the FeS_2 photo-Fenton system [20].

The investigation into the differences in catalytic activity among various crystal phases of FeS_2 is crucial for optimizing its application in environmental remediation. FeS_2 exists primarily in two distinct crystal forms: pyrite, which possesses a cubic lattice structure characterized by the space group Pa3, and marcasite, which has an orthorhombic structure with the space group Pnnm [21]. Recent studies highlight significant discrepancies in the catalytic performance of these phases. Nan et al. reported that the removal of 20 ppm RhB with marcasite as a Fenton reagent took 10 min reaction, while Xu et al. found that the removal of the same amount of RhB with pyrite in the Fenton system required 9-fold longer [22,23]. In contrast, Yi et al. reported that within the same reaction time, the removal rate of methyl orange using pyrite is 1.3 times that of marcasite [24]. These findings underscore the variability in catalytic activity among different FeS_2 crystal phases; however, the precise relationship between these crystalline structures and their respective catalytic efficiencies remains contentious.

The conflicting results indicate that the mechanisms governing the degradation capabilities of FeS_2 across different crystal phases and lattice structures are not yet fully understood. Furthermore, while mixed-phase catalysts have been shown to yield superior catalytic performance compared to their pure-phase counterparts generally, the specific behavior of mixed-phase FeS_2 warrants further exploration [25,26]. For example, well-established commercial TiO_2 (P25) is a blend of anatase and rutile phases. The enhanced photocatalytic activity of anatase-rutile composites is observed compared to anatase or rutile, which is attributed to the band alignment. For another instance, 1T/2H-MoS_2 is a blend of the triangular prism (2H) phase and the metal octahedral (1T) phase. The 1T/2H-MoS_2 exhibits accelerated PS activation under light irradiation relative to either 2H or 1 T-phased MoS_2. The activity enhancement is found to result from the promotion of charge generation and light absorption of the 2H phase, and the facilitation of PS activation at the edge sites of the 1T-MoS_2 phase [27]. These observations suggest that mixed-phase FeS_2 could potentially surpass the performance of its pure-phase components. However, the activation of H_2O_2 and subsequent degradation processes using mixed-phase FeS_2 remain insufficiently explored, and the underlying mechanisms of these interactions are still unclear. The purpose of this study is to clarify the mechanisms underlying the differences in catalytic activity among various crystal phases of FeS_2, specifically to explain why mixed-phase FeS_2 demonstrates superior catalytic performance compared to its pure-phase counterparts. Additionally, this research aims to elucidate the activation processes of H_2O_2 and the degradation of pollutants, ultimately identifying the mechanisms that enhance the catalytic performance of mixed-phase FeS_2 to address existing knowledge gaps.

In this study, pyrite-marcasite mixed-phase FeS_2 is prepared using a hydrothermal method. The Fenton degradation activity of this mixed-phase FeS_2 is compared with that of the pure-phase FeS_2. The mixed-phase FeS_2 demonstrates superior removal of the CIP pollutant in both pure water and actual wastewater. The effectiveness of Fenton degradation is examined by analyzing the generation of •OH radicals from H_2O_2. The study further explores how the conversion of Fe^{2+} to Fe^{3+} in marcasite and S^- to S^{2-} in pyrite can enhance the generation of •OH radicals from both H_2O_2 and H_2O in the mixed-phase FeS_2. More importantly, the research clarifies the role of the internal electric field (IEF), generated due to the work function difference between pyrite and marcasite, in facilitating the rapid regeneration of Fe^{2+} and S^- from the produced Fe^{3+} and S^{2-}, thereby sustaining the •OH generation process.

2. Experimental Section

2.1. Materials

Ferrous sulfate heptahydrate ($FeSO_4·7H_2O$), sodium thiosulfate pentahydrate ($Na_2S_2O_3·5H_2O$), L cysteine, glycol, Ferric chloride hexahydrate ($FeCl_3·6H_2O$), thiourea (NH_2CSNH_2), ciprofloxacin and anhydrous ethanol are purchased from the Sinopharm Chemical Reagent Co., Ltd. in analytic grade and used directly without further purification. The water with a resistance of 18.2 MΩ (Ultrapure water) is employed for all experiments unless otherwise specified.

2.2. Synthesis of FeS_2 with Different Crystal Phases

Note that specific combinations of reagents and conditions are essential and must not be altered [28–30].

2.2.1. Synthesis of Pyrite-FeS_2 (P-FeS_2)

Pyrite-FeS_2 is prepared by hydrothermal reaction. Typically, 0.081 g of $FeCl_3·6H_2O$ and 0.114 g of NH_2CSNH_2 are dissolved in 30 mL of ethylene glycol at room temperature. The solution is stirred for 45 min and then transferred to a 50 mL Teflon-lined steel autoclave. The autoclave is kept at 240 °C for 12 h. After the reaction and cooling to room temperature, the product is collected and alternately washed with water and ethanol. Finally, the obtained material is vacuum-dried at 80 °C for 12 h.

2.2.2. Synthesis of Marcasite-FeS_2 (M-FeS_2)

Marcasite-FeS_2 is also prepared by hydrothermal reaction. Typically, 0.404 g of $Fe(NO_3)_3·9H_2O$ and 0.6058 g of L-cysteine are dissolved in 20 mL of deionized water at room temperature. The mixture is stirred for 20 min and then added with 20 mL of glycerol. After an additional hour of stirring, the solution is transferred to a 50 mL Teflon-lined steel autoclave and reacted at 185 °C for 50 h. Once the reaction is complete, the resulting product is cooled to room temperature naturally and washed with water and ethanol. Finally, the obtained material is collected and vacuum-dried at 80 °C for 12 h.

2.2.3. Synthesis of Pyrite-Marcasite Mixed-Phase FeS_2 (P/M-FeS_2)

In a typical synthesis, $FeSO_4·7H_2O$ (0.010 mol) and $Na_2S_2O_3·5H_2O$ (0.010 mol) are dissolved in 25 mL deionized water. The mixture is stirred at room temperature for 10 min and transferred to a 50 mL teflon-lined stainless steel autoclave. The autoclave is kept at 200 °C for 24 h. After the reaction, the autoclave is naturally cooled to room temperature. Finally, the obtained product is centrifugated and rinsed with distilled water, carbon disulfide, and ethanol several times to obtain dark gray powder.

2.3. Evaluation of the Photo-Fenton Degradation Activity

The photo-Fenton degradation for CIP pollutants is evaluated with various phased FeS_2 under a 300 W xenon lamp ($\lambda > 300$ nm, Perfect Light, Beijing, China). A 10 mg FeS_2 is added into a 50 mL solution containing 50 ppm CIP, followed by 5 min of ultrasonic treatment to achieve a uniform suspension. The initial pH of the solution is measured to be approximately 4.1. Then 6 mM H_2O_2 is added to initiate the reaction. Samples are periodically withdrawn from the reaction solution using a syringe and filtered through a 0.22 μm Teflon filter. To quench the photo-Fenton reaction, 100 μL of ethanol is added to 900 μL of the sample. The photodegradation rate of CIP is estimated and fitted with the Langmuir–Hinshelwood first-order kinetic model.

Actual water samples from the lake and tap water are sourced from Jiangnan University (Wuxi, China), and the secondary-treated wastewater (SWW) is collected after secondary treatment (activated sludge and secondary clarifier) at a municipal wastewater treatment plant in Wuxi, China. Before use, all actual water samples are filtered through a 0.45 μm filter. Concentrations of CIP and degradation intermediates are analyzed using high-performance liquid chromatography (HPLC, Ultimate 3000RS, JASCO, Japan) with a C18 reversed-phase column and a mobile phase flow rate of 1.0 mL/min (methanol: 0.1% formic acid aqueous solution = 3:7, *v/v*). The concentration of CIP is detected at a wavelength of 272 nm.

2.4. Characterizations

X-ray diffraction (XRD) patterns are obtained using a Bruker D8-ADVANCE X-ray diffractometer (Germany) with Cu Kα1 radiation ($\lambda = 1.5406$ Å), operated at 40 kV and 40 mA. Scanning electron microscope

(Hitachi S-4800, Japan) and transmission electron microscope (JEM 2100plus, JEOL, Japan), respectively are the morphology and structure of the materials. Raman measurements are performed using a Smart Raman confocal-micro-Raman module equipped with a ×20 objective lens under backscattering geometry. This module, developed by the Institute of Semiconductors, Chinese Academy of Sciences, is coupled with a Horiba iHR550 spectrometer (HORIBA, America) featuring a 532 nm excitation laser and a charge-coupled device (CCD) detector. X-ray photoelectron spectroscopy (XPS) analysis is conducted using an AXIS Supra instrument (Kratos UK) with monochromatic Al Kα radiation (hv = 1486.6 eV, 225 W) as the X-ray source. The spectra are referenced to the C 1s peak at 284.8 eV for calibration. Radicals are examined under dark and light conditions using an electron paramagnetic resonance (ESR) spectrometer (Bruker EMXplus, Germany) with Xe lamp irradiation for 5 min. The morphology and surface potential of FeS_2 catalysts with different exposure planes are measured using an atomic force microscope (AFM) equipped with a Kelvin probe (AFM, SPM-9700HT, Shimadzu, Japan).

3. Results and Discussion

3.1. Morphology and Structure of the Prepared FeS_2 with Three Crystal Phases

FeS_2 is synthesized using hydrothermal methods, with adjustments made to the hydrothermal time and reactant compositions to achieve three distinct crystal phases. To investigate the unique properties of different reagents, we conducted a series of experiments. The results show that specific sources of iron and sulfur are critical and cannot be substituted arbitrarily (Figure S1). Figure 1a depicts the XRD patterns of FeS_2 catalysts, revealing these three phases. Pattern A exhibits characteristic peaks at 28.5°, 33.0°, 37.0°, 40.7°, and 56.2°, corresponding to the (111), (200), (210), (211), and (311) planes of pyrite (PDF#71-0053), confirming the successful synthesis of pure-phase pyrite FeS_2. Pattern B shows additional peaks at 25.9° and 52.1° relative to Pattern A, attributed to the (110) and (211) planes of marcasite (PDF#74-1051), indicating a mixture of pyrite and marcasite in the samples. Quantitatively, in Pattern B, pyrite (P-FeS_2) accounts for 63.9 wt%, while marcasite (M-FeS_2) constitutes 36.1 wt% (Supplementary Materials Table S1). Based on the dominant phase, Pattern B is denoted as P/M-FeS_2. Pattern C displays peaks solely at 25.9°, 31.2°, 33.1°, 33.2°, 37.3°, and 52.1°, and no peaks belonging to pyrite are observed, indicating the successful synthesis of pure-phase marcasite (PDF#74-1051).

Figure 1b displays the Raman spectra of the various phased FeS_2 catalysts. Curve A exhibits Raman peaks at 343, 380, and 432 cm^{-1}, The mode at 343 cm^{-1} corresponds to the displacement of S atoms perpendicular to the S-S bond (E_g), while the mode at 380 cm^{-1} is due to the in-phase S-S stretching vibration (A_g) of pyrite FeS_2, The weak band at 432 cm^{-1} can be attributed to the stretching T_g symmetry mode. The observations confirm the successful synthesis of pure-phased pyrite [31,32]. Compared to curve A, curve B exhibits additional peaks at 323 cm^{-1}, a characteristic peak of marcasite [33]. Curve C displays peaks solely at 323 and 380 cm^{-1}, corresponding to the A_g vibration modes of marcasite FeS_2. No peaks belonging to the vibrations of pyrite FeS_2 are observed, confirming the successful synthesis of pure marcasite [34]. The comparison of Raman peaks of the prepared three-phased FeS_2 shows a similar change tendency of phase content to that observed in the XRD, further verifying the phase content in the prepared FeS_2 catalyst. In addition, we conducted an in-depth BET surface area analysis, pore size distribution assessment, and UV-Vis DRS characterization of the three prepared catalysts (Figure S2).

SEM is measured for the P/M-FeS_2 to understand the structure of the mixed-phase sample better. The SEM image (Figure 1c) reveals that the P/M-FeS_2 catalyst comprises small nanoparticles (size 10–50 nm) loaded onto large nanosheets ranging in size from 100 nm to 500 nm. The results indicate that FeS_2 composites are nanostructured. According to literature reports, marcasite tends to form nanosheets, while pyrite readily forms nanoparticles due to its inherent lattice structure [35]. Therefore, in our case, the nanoparticles may be the pyrite phase, while the nanosheets may be the marcasite phase.

The high-resolution TEM images in Figure 1d provide additional evidence for confirming the phases. The images reveal for the nanosheets, the lattice fringe spacings of 0.326 nm are measured, corresponding to the (110) planes of marcasite, confirming the observed nanosheets are the marcasite phase, while for the nanoparticles, the lattice spacings of 0.310 nm are found, belonging to the (111) planes of pyrite, suggesting the nanoparticles are the pyrite phase. Figure 1d also reveals that in the P/M-FeS_2 sample, the pyrite nanoparticles expose their crystal surfaces of (111), and the marcasite nanosheets expose their crystal surfaces of (110).

The TEM observations of the prepared pure-phase FeS_2 further confirm the observed phase distribution in Figure 1c. Figure S3a shows the prepared pure-phase marcasite is the nanosheet structure, which ranges from about 100 to 500 nm. The inset HRTEM image reveals that the exposed surface of the marcasite nanosheet is the (110) plane. Figure S3b shows that the prepared pure-phase pyrite tends to form nanoparticles ranging in size from approximately 10 to 50 nm. Additionally, in the pure-phase pyrite, the exposed surface is determined to be the (111) planes, which is consistent with the surface exposed on the pyrite-phased nanoparticles in the P/M-FeS_2.

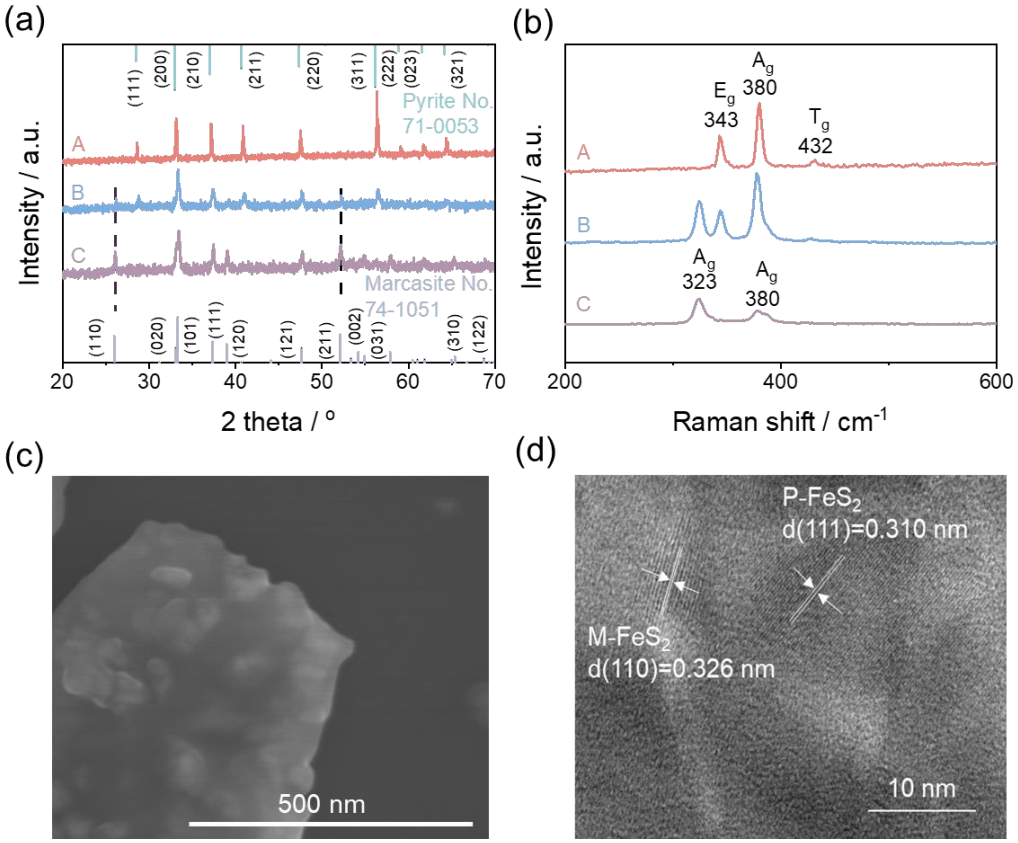

Figure 1. (**a**) XRD and (**b**) Raman of the prepared P-FeS_2, M-FeS_2 and P/M-FeS_2. (**c**) SEM and (**d**) HRTEM images of the prepared P/M-FeS_2 catalyst.

3.2. Photo-Fenton Degradation of CIP on Various Phased FeS_2

The photo-Fenton activity of various phased FeS_2 for organic pollutant degradation is investigated, with CIP chosen as the typical target contaminant. Figure 2a displays the photo-Fenton degradation of 50 ppm CIP with the three prepared FeS_2 catalysts with different phases. The results show that CIP exhibits 30% degradation after 10 min reaction in the presence of pure-phase P-FeS_2, indicating that P-FeS_2 exhibits weak capability for H_2O_2 activation. With pure-phase M-FeS_2, CIP requires ca. 10 min to achieve 90% of degradation. Using P/M-FeS_2, 90% of CIP is degraded within ca. 1.5 min. The degradation rate constant of P/M-FeS_2 (1.67 min^{-1}) is about 42 times higher than that of P-FeS_2 (0.04 min^{-1}) and 5.4 times higher than that of M-FeS_2 (0.31 min^{-1}) as shown in Figure S4a,b. Among reported photo-Fenton catalysts for CIP degradation, P/M-FeS_2 demonstrates the highest degradation activity, as listed in Table S2. This underscores the potential of using photo-Fenton P/M-FeS_2 for effective CIP degradation.

Next, the TOC removal efficiency of three prepared catalysts for CIP is compared (Figure S4c). It is observed that the P/M-FeS_2 catalyst exhibits the highest TOC removal efficiency. After 4 h reaction, the TOC removal rate for CIP in the P/M-FeS_2 system (73.2%) is 2.4 times higher than in the M-FeS_2 system (45.0%), and 136 times higher than in the P-FeS_2 system (4.0%) (Figure S4d). This demonstrates that the P/M-FeS_2 system also exhibits superior TOC removal capability, highlighting its strong mineralization capability.

In addition, we compare the photo-Fenton degradation activity in the P/M-FeS_2 system with that in the M/P-FeS_2 system where the majority phase is marcasite. The structure of the prepared M/P-FeS_2 catalyst is confirmed with Raman and XRD (Figure S5). The analysis reveals that the M/P-FeS_2 catalyst contains 32.3 wt% of pyrite and 67.7 wt% of marcasite (Supplementary Materials Table S1), indicating the majority phase in M/P-FeS_2 is marcasite. Subsequently, we conduct a CIP degradation test on M/P-FeS_2. The results show that the M/P-FeS_2 catalyst achieves a CIP degradation rate of 90% within 4 min, with a corresponding rate constant of 0.92 min^{-1}. After a 4 h reaction, the TOC removal rate of the M/P-FeS_2 system reaches 61.2% (Figure S4). On the contrary, in the P/M-FeS_2 system, the degradation rate constant of CIP (1.67 min^{-1}) and the removal rate of TOC (73.2%) are 1.8 times and 1.2 times of those in the M/P-FeS_2 system, respectively. These results indicate that with pyrite as a majority phase in the mixed-phase FeS_2, CIP is removed the most efficiently. According to the band gap and Mott-Schottky (Figure S6) measurements, The results show that E_{CB} of P/M-FeS_2, P-$FeS_2$and M-FeS_2 are -0.34, -

0.40 and -0.31 V (vs. NHE), respectively; the E_{VB} are 2.68, 1.41 and 3.29 V (vs. NHE), respectively.The BET specific surface areas (Supplemental materials, Table S3), transient photocurrent, and EIS spectra (Figure S7) of the three catalysts are determined. The results showed that neither the specific surface area nor the separation and recombination of electrons and holes showed a significant correlation with the degradation rate. Therefore, we speculate that the degradation activity may be influenced by other factors. Therefore, we speculate that the degradation activity may be influenced by other factors.

In addition, we compared the photoFenton degradation activity in commercial FeS_2 systems, and purchased natural FeS_2 structures are confirmed by XRD and SEM (Figure S8). Subsequently, we tested the CIP degradation of natural FeS_2. The results show that the activity of a natural FeS_2 catalyst is much lower than that of FeS_2 synthesized by the hydrothermal method.

To optimize the photo-Fenton reaction conditions in the P/M-FeS_2 system, we investigate the effects of the initial pH, the H_2O_2 concentration, and the catalyst dosage on the CIP degradation. The results reveal that P/M-FeS_2 retains high degradation efficiency across a wide pH range from acidic to weak basic conditions (3.2–8.2) (Figure S9). At a pH of 4.3, P/M-FeS_2 exhibits the highest photo-Fenton degradation activity for CIP. For the optimal H_2O_2 concentration, increasing the H_2O_2 concentration from 1 mM to 6 mM slightly improves the degradation rate from 60% to 99%. Still, a further increase (6–10 mM) leads to a slight decrease in the degradation rate from 99% to 20%. As reported in the literature, this is presumably because an excess of H_2O_2 addition may quench the generated •OH radicals in the P/M-FeS_2 system [36]. The optimal H_2O_2 concentration is 6 mM. Under the optimal pH and H_2O_2 concentration, FeS_2 dosage is then optimized to be 0.2 g/L. After optimizing the photo-Fenton reaction conditions, 6 mM H_2O_2, 0.2 g/L FeS_2, and 50 ppm CIP are chosen for the subsequent activity evaluation.

Figure 2b shows that in the P/M-FeS_2 photo-Fenton system, the degradation rate of CIP exceeds 95% within 2 min. In contrast, using only H_2O_2 results in a CIP removal rate of only 14% after 10 min reaction. Similarly, using only P/M-FeS_2 for degradation yields a CIP removal rate of 10% after 10 min reaction. When FeS_2 and H_2O_2 are both used but without light irradiation, the CIP removal percentage reaches 95% for 5 min reaction. CIP removal is challenging when using FeS_2 or H_2O_2 alone under light irradiation or using FeS_2 and H_2O_2 in the dark. The findings suggest that the effective removal of pollutants relies primarily on photo-Fenton activation of H_2O_2 by P/M-FeS_2.

Figures 2c and S10 show the selectivity of photo-Fenton degradation for various antibiotics using P/M-FeS_2. According to the literature, antibiotics are primarily classified based on their hydrophilic or hydrophobic properties and also divided by their charge (positive or negative) [37–40]. In our case, CIP and TC represent typical hydrophobic antibiotics, while OFX is chosen as a typical positively charged hydrophilic antibiotic, and SDZ is chosen as a typical negatively charged hydrophilic antibiotic. The results indicate that P/M-FeS_2 achieves a degradation percentage of 95% or higher for all tested antibiotics within 3 min, showcasing exceptional photo-Fenton degradation activity without selectivity.

After assessing the photo-Fenton degradation activity, we evaluate the stability of P/M-FeS_2. The stability of the P/M-FeS_2 system is assessed by continuously degrading pollutants without changing the P/M-FeS_2 catalyst. First, the reaction ceases when the CIP is degraded. Next, the solution is exposed to light for an additional 10 min to decompose any residual H_2O_2. The reaction solution is then removed by evaporation in a 50 °C water bath to ensure no loss of the P/M-FeS_2 amount. Finally, for the next degradation cycle, the CIP solution and H_2O_2 are re-added into the reactor to keep the initial concentrations the same as the previous cycle. Over 20 cycles, the P/M-FeS_2's activity is well maintained, and the CIP removal percentage remains at 95% within 2 min (Figure 2d). Analyses conducted before and after the degradation using Raman, XRD, SEM, and FTIR revealed that the morphology and structure of the catalyst remain unchanged after 20 cycles, indicating the morphology and structure are stable (Figure S11). In contrast, the stability of the P-FeS_2 and M-FeS_2 systems is evaluated, which shows quick decays just after 3 and 4 cycles, respectively (Figures S12 and S13). The high stability in P/M-FeS_2 may result from its mixed-phase structure, which will be discussed below.

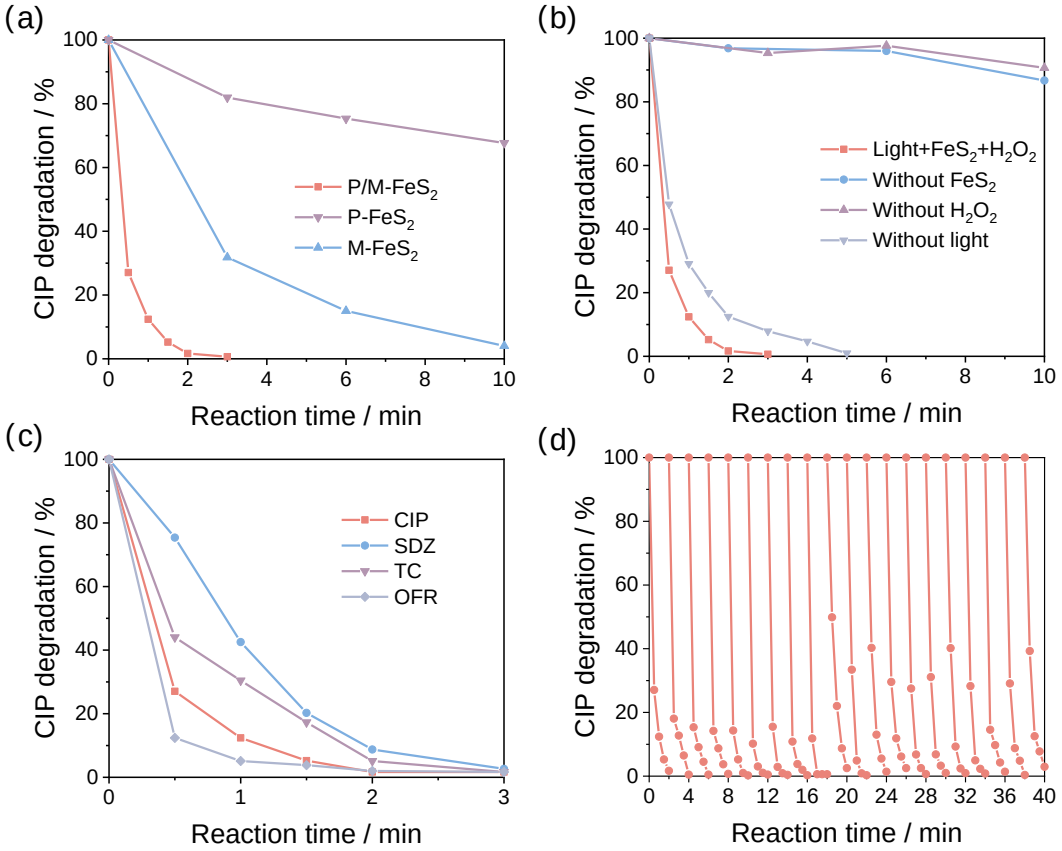

Figure 2. (**a**) Photo-Fenton Degradation of CIP with P-FeS_2, M-FeS_2, and P/M-FeS_2. (**b**) Degradation of CIP with H_2O_2 alone under light irradiation, P/M-FeS_2 alone under light irradiation, the P/M-FeS_2 Fenton system, and the P/M-FeS_2 photo-Fenton system. (**c**) Degradation of various antibiotics in the P/M-FeS_2 photo-Fenton system. (**d**) CIP degradation with P/M-FeS_2 for 20 cycles. Reaction conditions: 0.2 g L^{-1} FeS_2, 6 mM H_2O_2, 50 ppm CIP.

Actual wastewater typically contains high levels of inorganic ions and natural organic matter (NOMs), which can interfere with both pollutant degradation and the functioning of photo-Fenton systems [41,42]. Encouraged by the excellent photo-Fenton degradation activity with mixed-phase FeS_2, we evaluate the degradation in actual wastewater with common anions, cations, and NOMs.

Inorganic anions are known to quench free radicals, thereby influencing the concentration of oxidizing free radicals within a system [43]. Several inorganic anions commonly found in wastewater or natural water, such as chloride (Cl^-), bicarbonate (HCO_3^-), nitrate (NO_3^-), and sulfate (SO_4^{2-}), are chosen to assess their impact on the efficiency of CIP degradation in the P/M-FeS_2 photo-Fenton system. Sodium salts of these anions are added to the solution at a concentration of 5 mM to act as interfering agents. The anion concentration (5 mM) is selected based on the natural occurrence and available literature [44]. Figures 3a and S14 show the CIP degradation activity of P/M-FeS_2 in the presence of different anions. Within a 3 min reaction, the degradation rates of pollutants were 95%, 99%, and 99%, respectively, after adding Cl^-, NO_3^-, and SO_4^{2-}, similar to that without the presence of these anions (95% within 3 min reaction). These results indicate that adding these ions does not affect the CIP degradation activity in the P/M-FeS_2 photo-Fenton system significantly. However, the addition of bicarbonate inhibits pollutant degradation, resulting in only a 70% degradation percentage for 3 min reaction. HCO_3^- tends to react with •OH to form carbonate radicals (CO_3•$^-$) with a lower reduction potential (ca. 1.8 V) than that of hydroxyl radicals (2.8 V) [43]. This may reduce the pollutant degradation efficiency in the P/M-FeS_2 photo-Fenton system.

Figures 3b and S15 show the influence of different cations on the CIP degradation activity in the P/M-FeS_2 photo-Fenton system. According to the literature, the concentration of cations added in the experiment is set as 5 mM, which may be employed to assess the impact of cations-interfering substances on CIP degradation. Thus, chloride salts of Na^+, Mg^{2+}, Ca^{2+}, K^+, and NH_4^+ are used with a concentration of 5 mM. Within a 3 min photo-Fenton reaction, the degradation of CIP reaches 95%, 94%, 96%, 91%, and 99%, respectively, after adding Na^+, Mg^{2+}, Ca^{2+}, K^+, and NH_4^+. In our case, cations known to disrupt the photo-Fenton reaction are found to have minimal impact on the CIP degradation, highlighting the robustness of our system [45].

Humic acid (HA) is used as a representative NOM compound to assess the impact of natural organic matter (NOMs) on CIP degradation in the P/M-FeS_2 photo-Fenton system. The HA concentrations are typically ranging

from 5–10 ppm [46]. Figures 3c and S16 illustrate the influence of different concentrations of humic acid on CIP degradation in the P/M-FeS_2 photo-Fenton system. In the presence of 5 ppm HA, the degradation rate of CIP shows minimal change. While in the presence of 10 ppm HA, the CIP degradation is accelerated. This may be attributed to the phenol groups in HA acting as electron shuttles, thereby enhancing the electron transfer rate between H_2O_2 and the P/M-FeS_2, leading to increased •OH production [47]. The experiments demonstrate that the presence of humic acid exhibits negligible inhibitory effects on CIP degradation.

Figures 3d and S17 show the CIP degradation in the P/M-FeS_2 photo-Fenton system for different actual water sources. The degradation is evaluated in the secondary effluent from a wastewater treatment plant, tap water, and lake water. The results show that, under illuminated conditions, the degradation efficiency of CIP within 3 min is 99%, 91%, and 70%, respectively. The degradation performance of P/M-FeS_2 in secondary effluents from wastewater treatment plants is decreased, which may be due to the complexity of water quality in secondary wastewater. Different from ultra-pure water, there are small-sized colloidal nanoparticles in the treated secondary effluent, which can reduce the effective contact and reaction of Fenton's reagents (i.e., H_2O_2 and Fe^{2+}) through surface adsorption and other ways, thus reducing the efficiency of Fenton's reaction [48]. This may hinder CIP degradation in the photo-Fenton reaction. All the above results demonstrate that the degradation of CIP in the P/M-FeS_2 photo-Fenton system remains high in actual water bodies, despite the presence of inorganic ions and NOMs that could potentially interfere with the reaction.

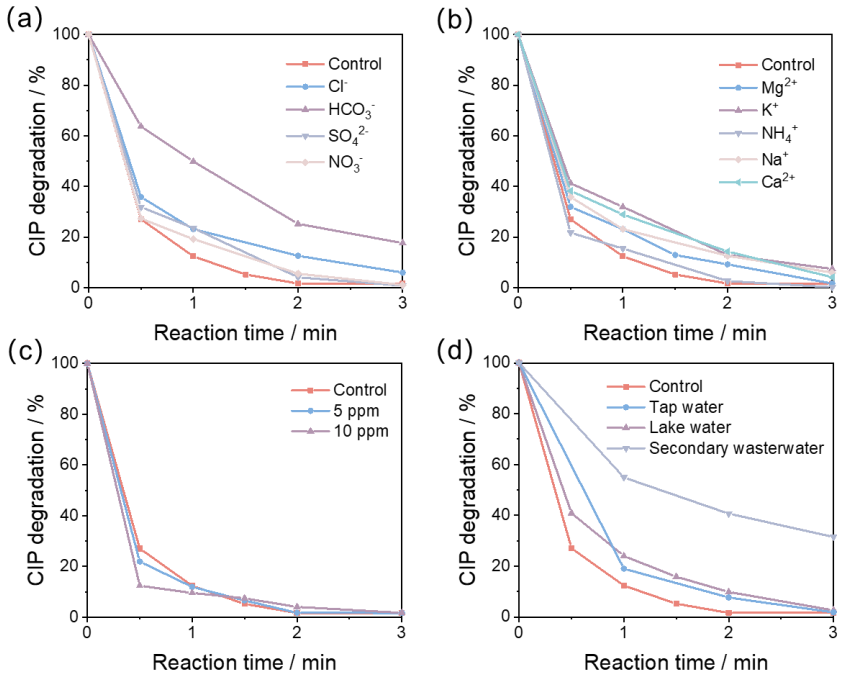

Figure 3. The CIP degradation in the presence of different anions (**a**), cations (**b**), and HA (**c**) in the P/M-FeS_2 photo-Fenton system. (**d**) The CIP degradation with different water sources in the P/M-FeS_2 photo-Fenton system. Reaction conditions: 0.2 g L^{-1} P/M-FeS_2, 6 mM H_2O_2, 50 ppm CIP. Control: Photo-Fenton degradation with P/M-FeS_2 in high-purity water.

The reactive oxygen species (ROS) are measured to further understand the excellent performance in the P/M-FeS_2 photo-Fenton system. To identify the main ROS responsible for CIP degradation, benzoquinone (BQ), L-histidine (L-His), and isopropyl alcohol (IPA) are used as scavengers for capturing superoxide radicals ($•O_2^-$), singlet oxygen ($^1O_2$), and hydroxyl radicals (•OH), respectively. As shown in Figure 4a, the addition of 1 mM of each scavenger exhibits different effects on CIP degradation. With the addition of BQ and L-His, negligible degradation rate decreases are observed, while with IPA addition, the degradation rate is significantly decreased. The results suggest that $•O_2^-$ and $^1O_2$ have a negligible impact on degradation, while •OH is the primary ROS involved in the CIP degradation.

Figure 4b illustrates the contribution of each ROS to the CIP degradation in the P/M-FeS_2 photo-Fenton system. The contribution of active species is calculated using the method detailed in the Supplementary Materials Experimental section. The results reveal that the contribution of •OH, $•O_2^-$, and $^1O_2$ to CIP degradation in the P/M-FeS_2 photo-Fenton system are 80.8%, 7.3%, and 11.9%, respectively. The order of contribution to the degradation rate is •OH > $^1O_2$ > $•O_2^-$, indicating that •OH plays the predominant role in degradation. The above results highlight

the critical role of •OH as the primary active species in the P/M-FeS_2 and H_2O_2 system, suggesting the observed superior activity originates from the H_2O_2 activation to generate •OH, similar to other reported Fe-based photo-Fenton system [49].

Figure 4c shows the EPR measurements of three prepared FeS_2 with different crystal phases using 5,5-dimethyl-1-pyrrolin-n-oxide (DMPO) as a trapping reagent. Under dark conditions and without H_2O_2 addition, there are negligible signals detected. After 3 min of illumination and with H_2O_2 addition, a set of equally spaced peaks emerged for all three prepared FeS_2. Such EPR signals are also detected in M/P-FeS_2 (Figure S18). The observed EPR peaks all exhibit an intensity ratio close to 1:2:2:1, which reveals that •OH is generated in the reaction system [50]. Note that the change tendency of the intensity of the •OH radicals correlates with the degradation activity change in different crystal phased FeS_2, confirming the •OH radicals are the main ROS for CIP degradation. In particular, P/M-FeS_2 produces the highest signal intensity for •OH radicals and exhibits the best degradation activity. These results indicate that compared to the pure-phased FeS_2, mixed-phase P/M-FeS_2 exhibits the most effective activation of H_2O_2.

Next, we examine whether the CIP is degraded by the photo-Fenton reaction or the photocatalytic reaction of mixed-phase P/M-FeS_2. According to the literature, during the photocatalytic degradation of pollutants, the degradation activity under oxygen conditions is generally significantly higher than that under air conditions [51]. This is because photogenerated electrons tend to reduce oxygen to form $\bullet O_2^-$, leaving h^+ to react with H_2O to produce •OH. As a result, higher O_2 concentration will accelerate the •OH generation. In contrast, in the photo-Fenton reaction, •OH mainly comes from the activation of H_2O_2 by the Fenton reagents and thus higher O_2 concentration will not accelerate the •OH generation [52]. In our case, we conduct CIP degradation under different atmospheres (O_2, Ar, Air). The results show that the CIP degradation in both O_2 and Ar reaches ca. 99% after 3 min, comparable to that in air, suggesting the CIP degradation is primarily due to photo-Fenton reaction rather than photocatalytic reaction. Additionally, we attempted to add KI known as an h^+ capture reagent, into the reaction system (Figure S19). In that case, no significant decrease in the CIP degradation is observed, indicating the photogenerated h^+ is not the main ROS for CIP degradation. This again confirms the observed degradation is not mainly due to the photocatalytic reaction.

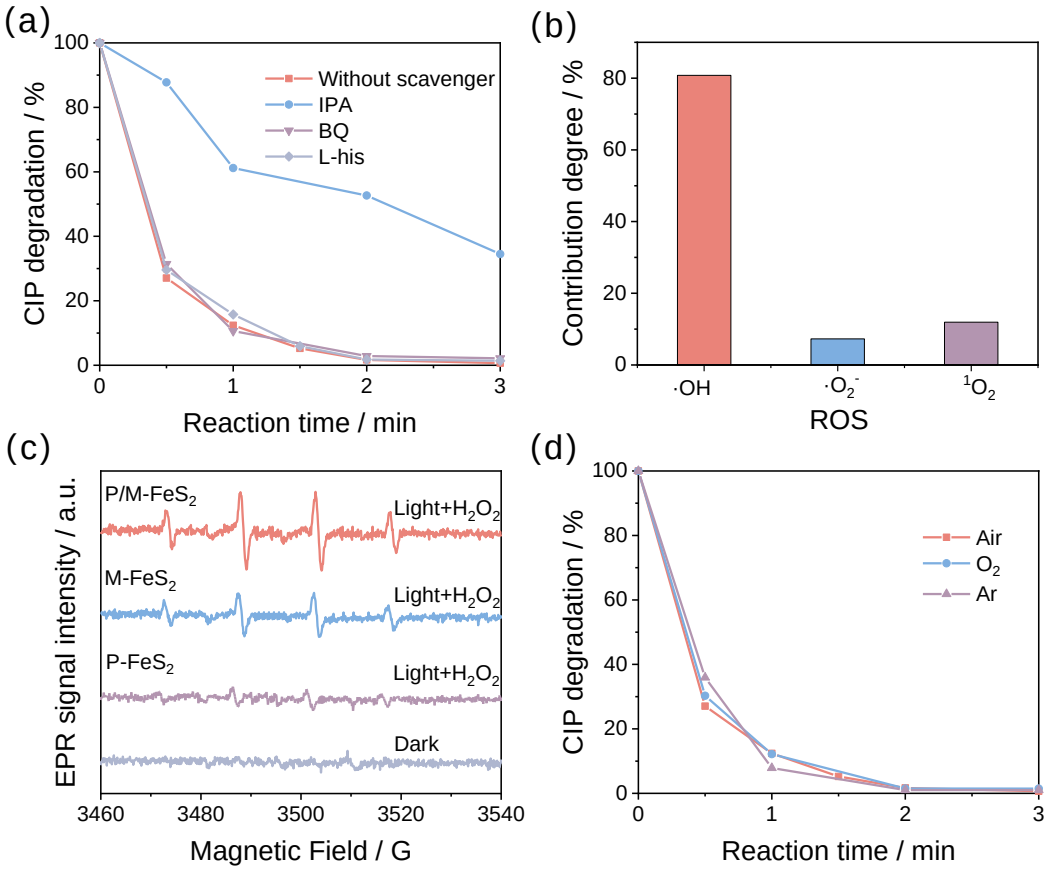

Figure 4. (**a**) Degradation curves of CIP in the presence of different ROS scavengers. (**b**) Contribution of Reactive Oxygen Species (ROS) to the photo-Fenton degradation of CIP. (**c**) EPR measurement for different crystal phased FeS_2 using 5,5-Dimethyl-1-pyrroline-N-oxide as an •OH-trapping reagent. (**d**) CIP degradation under different

atmospheres in the P/M-FeS_2 photo-Fenton system. Reaction conditions: 0.2 g L^{-1} catalyst, 6 mM H_2O_2, 50 ppm CIP.

3.3. Enhancement Mechanism with P/M-FeS_2

To clarify the factors contributing to the excellent activity of P/M-FeS_2, we investigate the surface structure of FeS_2 before and after CIP degradation. The valence states of Fe and S elements in P-FeS_2, M-FeS_2, and P/M-FeS_2 before and after the reaction are analyzed using XPS, as shown in Figure 5. In all the high-resolution Fe 2p spectra, Fe 2p orbitals exhibit the main peak and the corresponding satellite one as reported [53]. The main peaks are fitted with two sets of individual peaks located at 708.5 eV and 721.0 eV, and 707.2 eV and 719.8 eV, respectively. The peak at 708.5 eV and 721.0 eV, respectively, corresponds to the binding energy of Fe 2p3/2 and Fe 2p1/2 of Fe(III) as reported in Fe(III) hydroxide [54]. The peaks at 707.2 eV and 719.8 eV are attributed to Fe 2p3/2 and Fe 2p1/2 of Fe(II), respectively [55,56]. In all the high-resolution S 2p spectra, peaks at 162.7 eV, 163.8 eV, 164.8, and 168.8 eV are observed, corresponding to S_2^{2-} (S 2p3/2) and S_2^{2-} (S 2p1/2), S(0), and SO_4^{2-}, respectively [57–59].

The detailed changes of FeS_2 with different crystal phases before and after the degradation are then analyzed. Figure 5a shows that the Fe^{2+} content in Fe species in M-FeS_2 decreases from 52.3% to 38.8%, while the Fe^{3+} content increases from 47.7% to 61.8%. At the same time, the S_2^{2-} content in S species remains relatively stable (Figure 5b). This indicates that in M-FeS_2, Fe^{2+} is transferred to Fe^{3+} in the photo-Fenton reaction process, which promotes the formation of •OH and the degradation of CIP.

Figure 5c shows in P-FeS_2, before and after the degradation, Fe^{2+} and Fe^{3+} contents are barely changed. Meanwhile, Figure 5d illustrates that the S_2^{2-} content in S species in P-FeS_2 decreases from 62.7% to 57.7%. This indicates that S_2^{2-} participated in the Fenton reaction. Note that no change in the S-peak is observed in M-FeS_2, suggesting that the reaction pathways of the two phases of FeS_2 are different. Additionally, P-FeS_2 shows a new S-peak at 161.35 eV after the reaction, indicating the presence of iron sulfide (FeS) [60]. The change in the XPS S peaks rather than Fe peaks suggests that in P-FeS_2, the S_2^{2-} species induce the Fenton reaction rather than Fe^{2+}. In Figure S20, P-FeS_2 is reacted in water with Ar bubbling. By excluding H_2O_2 and O_2, a certain amount of •OH is still detected, demonstrating that in P-FeS_2, S_2^{2-} can oxidize H_2O to produce •OH, similar to what Li et al. reported [61].

XPS analysis shows that different crystal phases lead to different •OH generation pathways. In the pyrite phase, S_2^{2-} oxidizes H_2O to produce S^{2-} and •OH radicals, while in the marcasite phase, Fe^{2+} reduces H_2O_2 to produce Fe^{3+} and •OH radicals. The reaction difference is likely related to the exposed surface in each phase containing different Fe and S ratios (i.e., Fe: S = 1: 10.5 in pristine M-FeS_2 and 1: 27.6 in pristine P-FeS_2, Supplementary Materials Table S4) as discussed below. Analysis of XPS results indicated differing initial compositions: P-FeS_2 predominantly exposed S_2^{2-}, whereas M-FeS_2 predominantly exposed Fe^{2+}, and reacted with H_2O and H_2O_2, respectively.

Figure 5e shows that in the mixed-phase P/M-FeS_2, the Fe^{2+} and Fe^{3+} contents change from 81.3% to 81.0% and from 18.73% to 19.0% respectively, before and after degradation, barely compared to those in M-FeS_2, while in Figure 5f, the S_2^{2-} content remains unchanged. The slight change of Fe and S indicates that the valence state of the element in P/M-FeS_2 is stable during the Fenton reaction, probably due to the interactions between the two phases. The synergistic combination of these two crystal phases maximizes the respective advantages of each pure-phase catalyst.

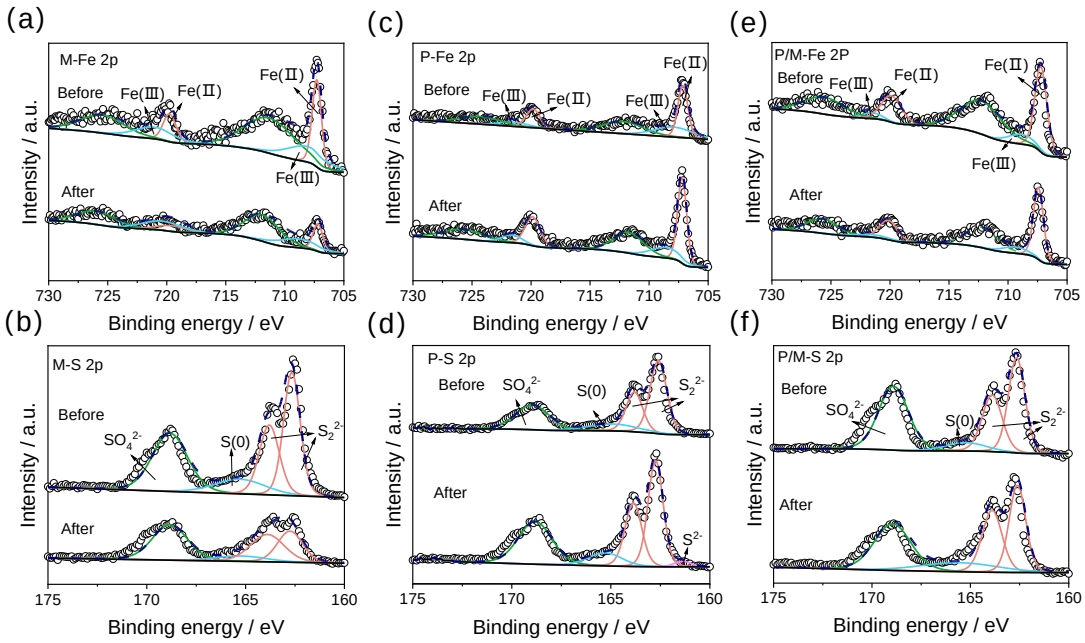

Figure 5. XPS spectra for Fe 2p and S 2p peaks in the prepared FeS_2 with different crystal phases before and after the degradation. (**a**,**b**) M-FeS_2, (**c**,**d**) P-FeS_2, and (**e**,**f**) P/M-FeS_2.

According to XPS analysis, P-FeS_2 exhibits higher exposure of S species relative to M-FeS_2, while M-FeS_2 exhibits higher exposure of Fe species relative to P-FeS_2. The different exposure will cause the marcasite and pyrite phases to react with H_2O_2 and H_2O, respectively, during the degradation process. To better understand the reasons, we create the structure models for the (111) surface exposed on P-FeS_2 and (110) surface exposed on M-FeS_2 according to the HRTEM observations (Figure 2d). The surface is optimized by the DFT method detailed in the Supplementary Materials Experimental section. The optimized (111) surface on P-FeS_2 and (110) surface on M-FeS_2 are shown in Figure 6a. Figure 6a and Table S5 show the Fe and S ratios are 1:3 and 1:2 for P-FeS_2 and M-FeS_2, respectively, the tendency of which is consistent with the XPS analysis. This confirms that it's the surface structure difference leads to the change of pathway of •OH generation in each phase.

The adsorption energy of H_2O and H_2O_2 on the two surfaces are calculated by optimizing the surface structures (Figure 6b,c), respectively. Figure 6d displays the calculated adsorption energies of H_2O and H_2O_2, respectively, on the (111) surface of P-FeS_2 and (110) surface of M-FeS_2. For P-FeS_2, the adsorption energy of H_2O is −3.08 eV, while that of H_2O_2 is −2.02 eV, indicating stronger adsorption of H_2O on P-FeS_2 compared to H_2O_2. This is probably because the small H_2O molecules tend to form more hydrogen bonds with the exposed S surface relative to that in the large H_2O_2 molecules. (Figure S21) In contrast, on the (110) surface in M-FeS_2, the adsorption energy of H_2O is −2.14 eV, while that of H_2O_2 is −2.69 eV, indicating H_2O_2 shows a stronger adsorption than H_2O. This may be due to Fe exposure on the (110) surface of M-FeS_2. Therefore, the different S and Fe exposure on the (111) surface in P-FeS_2 and (110) surface in M-FeS_2, respectively, will lead to the different preference adsorption of H_2O and H_2O_2 on the given surface. This may cause the H_2O_2 reduction in the marcasite phase and H_2O oxidation in the pyrite phase, confirming the XPS observations.

The contact angles of H_2O and H_2O_2 on P-FeS_2 and M-FeS_2 are measured to confirm the interaction difference between each phase. Figure 6e shows that the contact angle of H_2O_2 on P-FeS_2 is 54.2°, while the contact angle of H_2O is 21.6°. Figure 6f shows on M-FeS_2, the contact angle of H_2O_2 is 29.3°, while that of H_2O is 42.0°. These results indicate that H_2O_2 has a lower affinity on P-FeS_2 than H_2O, while the affinity for H_2O_2 and H_2O on M-FeS_2 is inverted. These findings experimentally confirm the interactions of H_2O and H_2O_2 on each FeS_2 phase are different and explain that P-FeS_2 reacts preferentially with H_2O to form •OH, while M-FeS_2 tends to react with H_2O_2 to form •OH.

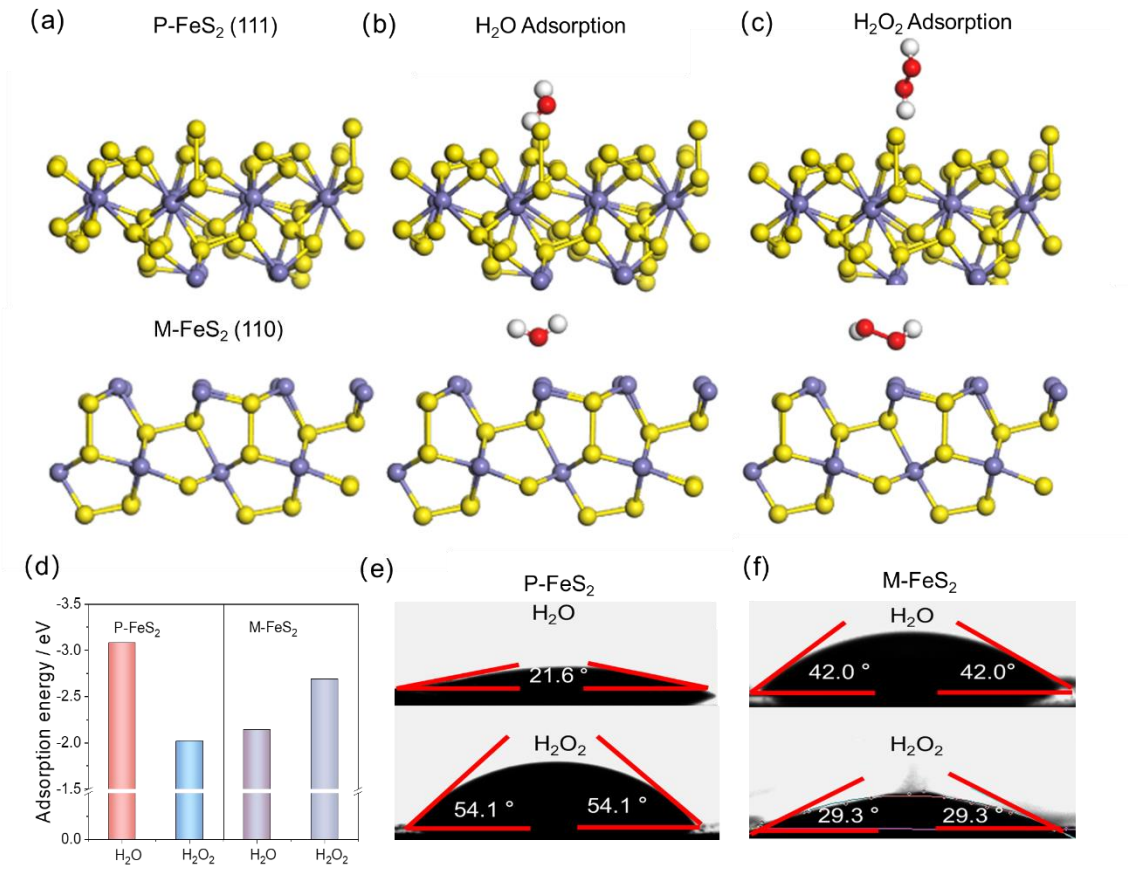

Figure 6. Crystal structure of (**a**) bare surface, (**b**) the H_2O adsorbed surface, and (**c**) the H_2O_2 adsorbed surface of the P-FeS_2 exposing (111) planes and M-FeS_2 exposing the (110) planes, respectively. (**d**) Calculated adsorption energies for H_2O and H_2O_2 on the (111) surface of P-FeS_2 and the (110) surface of M-FeS_2, respectively. Contact angle measurements of H_2O and H_2O_2 on P-FeS_2 (**e**) and M-FeS_2 (**f**), respectively.

Figure 7 shows the calculated and measured work functions (Φ) of (111) surfaces of P-FeS_2 and (110) surfaces of M-FeS_2. The work functions obtained from the DFT calculations are based on the optimized surfaces (Figure 6a). The calculated work functions of (111) surfaces in P-FeS_2 and (110) surfaces in M-FeS_2 surfaces are 4.394 eV and 3.18 eV, respectively. The Fermi energy level can be calculated based on the work function and vacuum energy (i.e., $E_F = E_{vac} - \Phi$). Since the vacuum energy is 0 eV for both P-FeS_2 and M-FeS_2, the higher work function of P-FeS_2 than that of M-FeS_2, indicating that the Fermi energy level for P-FeS_2 is lower than that for M-FeS_2. The results indicate that when forming the mixed-phase P/M-FeS_2 between the (111) surfaces of P-FeS_2 and (110) surfaces of M-FeS_2 surfaces, the electrons tend to transfer from M-FeS_2 to P-FeS_2 due to the difference in the Fermi energy level. The electron transfer may cause the formation of an IEF between the two phases, as reported in the literature [62].

To further confirm the difference in the work functions between P-FeS_2 and M-FeS_2, KPFM measurements are employed, which quantify the work function of a sample by measuring the contact potential difference (CPD) on the sample surface. Since CPD can be calculated as $CPD = \Phi_{tip} - \Phi_{sample}$, the work function of the sample (Φ_{sample}) can be obtained ($\Phi_{sample} = \Phi_{tip} - CPD_{sample}$). To calculate the work function of the sample, the work function (Φ_{tip}) of the conducting probe must first be determined. This process is accomplished by calibrating the probe with newly cut highly oriented pyrolytic graphite (Φ_{HOPG}). Given that the work function of Φ_{HOPG} is 4.65 eV, the Φ_{tip} can be calculated by measuring the contact potential difference (CPD_{HOPG}) on the HOPG surface ($CPD_{HOPG} = \Phi_{tip} - \Phi_{HOPG}$) [63]. The CPD_{HOPG} is measured as −0.20 V and −0.45 V during the measurement of P-FeS_2 and M-FeS_2, respectively. Figure 7c,d show that the measured work functions of P-FeS_2 and M-FeS_2 obtained by KPFM are 4.42 eV and 4.00 eV, respectively. The relationship between works functions for each crystal phase is consistent with the DFT calculation results, confirming the electron transfer direction is from M-FeS_2 to P-FeS_2.

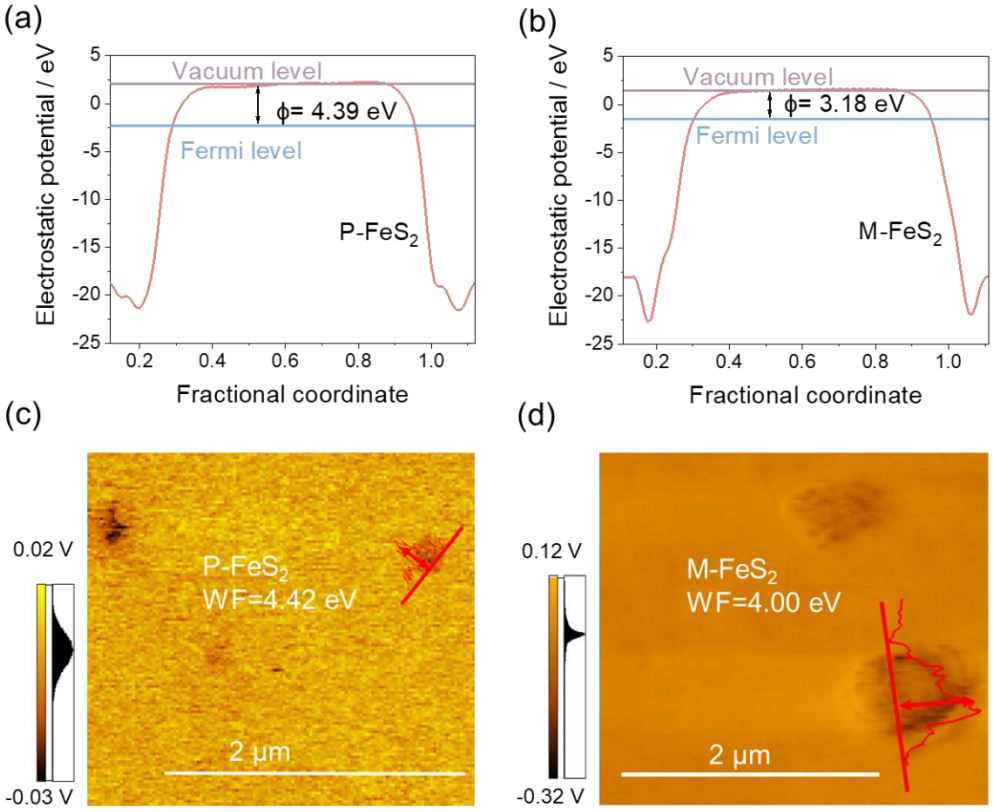

Figure 7. The work function obtained by the DFT calculations (**a**,**b**) and the KPFM measurements (**c**,**d**) of the (111) surface of P-FeS_2 and the (110) surface of M-FeS_2, respectively.

Figure 8 summarizes the influence of work function difference between P-FeS_2 and M-FeS_2 on the degradation activity enhancement of the mixed-phase P/M-FeS_2. Before contact, P-FeS_2 and M-FeS_2 show different Fermi energy levels. M-FeS_2 exhibits a higher Fermi energy level relative to P-FeS_2 due to the work function difference, which may drive the electrons to transfer from M-FeS_2 and P-FeS_2 when forming the interfaces between the two phases. After forming mixed-phase P/M-FeS_2, M-FeS_2 contacts P-FeS_2, and electrons will spontaneously transfer from M-FeS_2 to P-FeS_2 until the Fermi levels of both semiconductors equilibrate. Such an electron transfer may cause the formation of IEF between the two phases (Figure S22), and the direction of IEF is from M-FeS_2 to P-FeS_2.

During the CIP degradation reaction, H_2O reacts preferentially with P-FeS_2 to form S^{2-} and •OH, while H_2O_2 tends to react with M-FeS_2 to generate •OH and Fe^{3+} due to the difference in surface structure and calculated adsorption energy (Figures 6 and 7). The IEF between the interface between M-FeS_2 to P-FeS_2 will drive the excess electrons on S^{2-} of P-FeS_2 to transfer to Fe^{3+} of M-FeS_2, causing the regeneration of S_2^{2-} and Fe^{2+} in each phase as demonstrated by the XPS (Figure 5). The •OH generation from both H_2O_2 and H_2O and the rapid regeneration of active sites for the Fenton reaction may result in the high activity and stability of mixed-phase P/M-FeS_2.

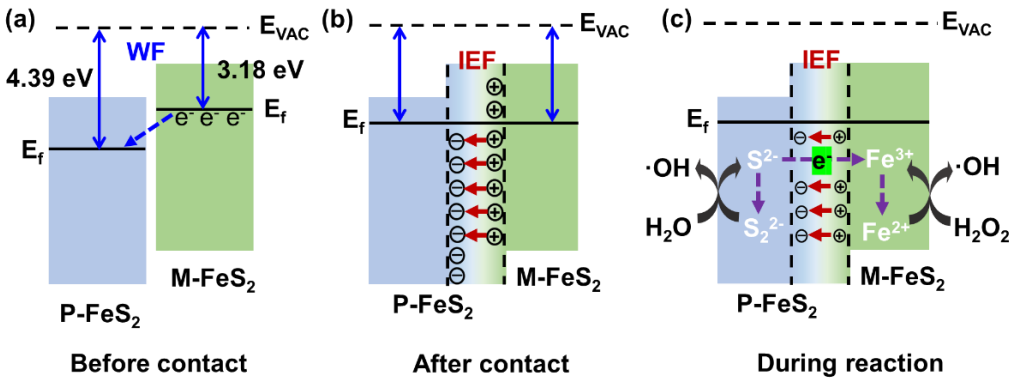

Figure 8. (**a**) The work function of P-FeS_2 and M-FeS_2 before contact. (**b**) The IEF formed at the interface of P/M-FeS_2 after contact. (**c**) The reaction mechanism on P/M-FeS_2 affected by the IEF.

4. Conclusions

In conclusion, FeS_2 with pyrite, marcasite, and pyrite-marcasite mixed phases are successfully synthesized through hydrothermal reactions. Among these, the mixed-phase P/M-FeS_2 exhibits significantly higher Fenton degradation activity for CIP pollutants compared to pure P-FeS_2 and M-FeS_2. This enhanced performance is attributed to the efficient generation of •OH radicals on the P/M-FeS_2 surface. The results demonstrate that in P/M-FeS_2, •OH radicals are generated from both H_2O_2 and H_2O on the M-FeS_2 and P-FeS_2 components, respectively, owing to differences in surface structure and adsorption energy. Moreover, the data illustrate that in P/M-FeS_2, the internal electric field formed between M-FeS_2 and P-FeS_2 due to their distinct work functions facilitates rapid regeneration of active sites S_2^{2-} in P-FeS_2 and Fe^{2+} in M-FeS_2), thereby sustaining the Fenton reaction. The combination of multiple pathways for •OH generation and the rapid regeneration of active sites likely accounts for the high activity and stability of the mixed-phase P/M-FeS_2. The development of mixed-phase FeS_2 as a high-activity Fenton reagent and the elucidation of its interfacial electric field-related mechanism for enhancing activity could offer valuable insights for the future design of Fenton catalysts aimed at the efficient degradation of antibiotic pollutants.

Supplementary Materials: Extra TEM, SEM, XRD, Raman, and KPFM experimental data of different crystal-phased FeS_2, as well as additional Fenton reaction activity, and the DFT calculation models.

Author Contributions: Conceptualization, methodology, writing—original draft, H.L.; visualization and investigation, Y.S. and S.D.; supervision, calculation, methodology, writing—review & editing, C.P. All authors have read and agreed to the published version of the manuscript.

Funding: This research was supported by the National Natural Science Foundation of China (22172065, 22476071), and the Special Fund Project of Jiangsu Province for Scientific and Technological Innovation in Carbon Peaking and Carbon Neutrality (BK20220023).

Data Availability Statement: Data will be made available on request.

Conflicts of Interest: The authors declare that there are no declarations of interest.

References

1. Lin, Y.; Wang, Y.; Shi, C.; Zhang, D.; Liu, G.; Chen, L.; Yuan, B.; Hou, A.; Zou, D.; Liu, X.; et al. Degradation of ciprofloxacin by a constitutive g-C_3N_4/BiOCl heterojunction under a persulfate system. *RSC Adv.* **2023**, *13*, 4361–4375. https://doi.org/10.1039/d2ra06500b.
2. Ferreira, V.R.A.; Amorim, C.L.; Cravo, S.M.; Tiritan, M.E.; Castro, P.M.L.; Afonso, C.M.M. Fluoroquinolones biosorption onto microbial biomass: Activated sludge and aerobic granular sludge. *Int. Biodeterior. Biodegrad.* **2016**, *110*, 53–60. https://doi.org/10.1016/j.ibiod.2016.02.014.
3. El-Sheikh, S.M.; Hakki, A.; Ismail, A.A.; Badawy, W.A.; Bahnemann, D.W. Highly active non-metals doped mixed-phase TiO_2 for photocatalytic oxidation of ibuprofen under visible light. *J. Photochem. Photobiol. A Chem.* **2017**, *346*, 530–540. https://doi.org/10.1016/j.jphotochem.2017.07.004.
4. Khedr, T.M.; El-Sheikh, S.M.; Abdeldayem, H.M.; Ismail, A.A.; Kowalska, E.; Bahnemann, D.W. A comparative study of microcystin-LR degradation by UV-A, solar and visible light irradiation using bare and C/N/S-modified titania. *Catalysts* **2019**, *9*, 877. https://doi.org/10.3390/catal9110877.
5. Yi, K.; Wang, D.; Yang, Q.; Li, X.; Chen, H.; Sun, J.; An, H.; Wang, L.; Deng, Y.; Liu, J.; Zeng, G. Effect of ciprofloxacin on biological nitrogen and phosphorus removal from wastewater. *Sci. Total Environ.* **2017**, *605*, 368–375. https://doi.org/10.1016/j.scitotenv.2017.06.215.
6. Zheng, J.; Zhang, P.; Li, X.; Ge, L.; Niu, J. Insight into typical photo-assisted AOPs for the degradation of antibiotic micropollutants: Mechanisms and research gaps. *Chemosphere* **2023**, *343*, 140211–140211. https://doi.org/10.1016/j.chemosphere.2023.140211.
7. Khedr, T.M.; El-Sheikh, S.M.; Kowalska, E.; Abdeldayem, H.M. The synergistic effect of anatase and brookite for photocatalytic generation of hydrogen and diclofenac degradation. *J. Environ. Chem. Eng.* **2021**, *9*, 106566. https://doi.org/10.1016/j.jece.2021.106566.
8. Xiong, J.-Q.; Kurade, M.B.; Kim, J.R.; Roh, H.-S.; Jeon, B.-H. Ciprofloxacin toxicity and its co-metabolic removal by a freshwater microalga Chlamydomonas mexican. *J. Hazard. Mater.* **2017**, *323*, 212–219. https://doi.org/10.1016/j.jhazmat.2016.04.073.
9. Wang, Y.; Chen, J.; Gao, J.; Meng, H.; Chai, S.; Jian, Y.; Shi, L.; Wang, Y.; He, C. Selective electrochemical H_2O_2 generation on the graphene aerogel for efficient electro-Fenton degradation of ciprofloxacin. *Sep. Purif. Technol.* **2021**, *272*, 118884. https://doi.org/10.1016/j.seppur.2021.118884.
10. Walkowiak, A.; Wolski, L.; Ziolek, M. The influence of ferrocene anchoring method on the reactivity and stability of SBA-15-based catalysts in the degradation of ciprofloxacin via photo-Fenton process. *RSC Adv.* **2023**, *13*, 8360–8373.

https://doi.org/10.1039/d3ra00188a.

11. Nie, X.; Li, G.; Li, S.; Luo, Y.; Luo, W.; Wan, Q.; An, T. Highly efficient adsorption and catalytic degradation of ciprofloxacin by a novel heterogeneous Fenton catalyst of hexapod-like pyrite nanosheets mineral clusters. *Appl. Catal. B-Environ.* **2022**, *300*, 120734. https://doi.org/10.1016/j.apcatb.2021.120734.
12. Yu, Y.; Sun, Y.; Zhou, Y.; Xu, A.; Xu, Y.; Huang, F.; Zhang, Y. The behavior of surface acidity on photo-Fenton degradation of ciprofloxacin over sludge derived carbon: Performance and mechanism. *J. Colloid Interface Sci.* **2021**, *597*, 84–93. https://doi.org/10.1016/j.jcis.2021.03.156.
13. Bossmann, S.H.; Oliveros, E.; Göb, S.; Siegwart, S.; Dahlen, E.P.; Payawan, L.; Straub, M.; Wörner, M.; Braun, A.M. New evidence against hydroxyl radicals as reactive intermediates in the thermal and photochemically enhanced fenton reactions. *J. Phys. Chem. A* **1998**, *102*, 5542–5550. https://doi.org/10.1021/jp980129j.
14. Hakimi, M.; Alikhani, M.J.J. o. I.; Polymers, O.; Materials, Characterization of α-Fe_2O_3 nanoparticles prepared from a new [Fe (Ofloxacin) $2Cl_2$] precursor: A heterogeneous photocatalyst for removal of methylene Blue and ciprofloxacin in water. *J. Inorg. Organomet. Polym. Mater.* **2020**, *30*, 504–512.
15. Qiu, B.; Li, Q.; Shen, B.; Xing, M.; Zhang, J. Stöber-like method to synthesize ultradispersed Fe_3O_4 nanoparticles on graphene with excellent Photo-Fenton reaction and high-performance lithium storage. *Appl. Catal. B: Environ.* **2016**, *183*, 216–223. https://doi.org/10.1016/j.apcatb.2015.10.053.
16. Wang, X.; Wang, J.; Cui, Z.; Wang, S.; Cao, M.J.R. Facet effect of α-Fe_2 O_3 crystals on photocatalytic performance in the photo-Fenton reaction. *RSC Adv.* **2014**, *4*, 34387–34394. https://doi.org/10.1039/C4RA03866E.
17. Holmes, P.R.; Crundwell, F.K. The kinetics of the oxidation of pyrite by ferric ions and dissolved oxygen: An electrochemical study. *Geochim. Cosmochim. Acta* **2000**, *64*, 263–274. https://doi.org/10.1016/s0016-7037(99)00296-3.
18. Liu, W.; Wang, Y.; Ai, Z.; Zhang, L. Hydrothermal Synthesis of FeS_2 as a High-Efficiency Fenton Reagent to Degrade Alachlor via Superoxide-Mediated Fe(II)/Fe(III) Cycle. *ACS Appl. Mater. Interfaces* **2015**, *7*, 28534–28544. https://doi.org/10.1021/acsami.5b09919.
19. Zeng, L.; Gong, J.; Dan, J.; Li, S.; Zhang, J.; Pu, W.; Yang, C. Novel visible light enhanced Pyrite-Fenton system toward ultrarapid oxidation of p-nitrophenol: Catalytic activity, characterization and mechanism. *Chemosphere* **2019**, *228*, 232–240. https://doi.org/10.1016/j.chemosphere.2019.04.103.
20. Zhang, F.; Liu, J.; Yue, H.; Cheng, G.; Xue, X. Enhanced photo-Fenton catalytic activity by spherical FeS_2 nanoparticles and photoelectric property of hybrid FeS_2/rGO. *Vacuum* **2021**, *192*, 110433. https://doi.org/10.1016/j.vacuum.2021.110433.
21. Schmokel, M.S.; Bjerg, L.; Cenedese, S.; Jorgensen, M.R.V.; Chen, Y.-S.; Overgaard, J.; Iversen, B.B. Atomic properties and chemical bonding in the pyrite and marcasite polymorphs of FeS_2: A combined experimental and theoretical electron density study. *Chem. Sci.* **2014**, *5*, 1408–1421. https://doi.org/10.1039/c3sc52977k.
22. Huang, X.; Wei, J.; Jiang, X.; Nan, Z. FeS_2/SiO_2 mesoporous hollow spheres formation and catalytic properties in the Fenton reaction. *Mater. Lett.* **2020**, *277*, 128408. https://doi.org/10.1016/j.matlet.2020.128408.
23. Diao, Z.-H.; Liu, J.-J.; Hu, Y.-X.; Kong, L.-J.; Jiang, D.; Xu, X.; Technology, P. Comparative study of Rhodamine B degradation by the systems pyrite/H_2O_2 and pyrite/persulfate: Reactivity, stability, products and mechanism. *Sep. Purif. Technol.* **2017**, *184*, 374–383. https://doi.org/10.1016/j.seppur.2017.05.016.
24. Lin, Y.; Li, J.; Chen, S.; Zhou, H.; Shu, Y.; Tang, L.; Long, Q.; Zhang, P.; Huang, Y.; Technology, P. In situ construction of pyrite-marcasite-magnetite composite via FeS_2 phase transformation and oxidation for the synergistic degradation of methyl orange and Cr (VI). *Sep. Purif. Technol.* **2023**, *308*, 122764. https://doi.org/10.1016/j.seppur.2022.122764.
25. Cui, P.; Hu, Y.; Zheng, M.; Wei, C. Enhancement of visible-light photocatalytic activities of $BiVO_4$ coupled with g-C_3N_4 prepared using different precursors. *Environ. Sci. Pollut. Res.* **2018**, *25*, 32466–32477. https://doi.org/10.1007/s11356-018-3119-3.
26. El-Sheikh, S.M.; Khedr, T.M.; Amer Hakki, K .; Ismail, A.A.; Badawy, W. A.; Bahnemann, D.W.Visible light activated carbon and nitrogen co-doped mesoporous TiO_2 as efficient photocatalyst for degradation of ibuprofen. *Sep. Purif*. **2017,** 258–268, 1383–5866**.** https://doi.org/10.1016/j.seppur.2016.09.034.
27. Chen, Y.; Zhang, G.; Ji, Q.; Liu, H.; Qu, J. Triggering of Low-Valence Molybdenum in Multiphasic MoS_2 for Effective Reactive Oxygen Species Output in Catalytic Fenton-like Reactions. *ACS Appl. Mater. Interfaces* **2019**, *11*, 26781–26788. https://doi.org/10.1021/acsami.9b05978.
28. Liu W, Wang Y, Ai Z; et al. Hydrothermal synthesis of FeS_2 as a high-efficiency Fenton reagent to degrade alachlor via superoxide-mediated Fe (II)/Fe (III) cycle. *ACS Appl. Mater. Interfaces* **2015**, *51*, 28534–28544. https://doi.org/10.1021/acsami.5b09919.
29. Wu, X.; Zhao, H.; Xu, J. Rational synthesis of marcacite FeS_2 hollow microspheres for high-rate and long-life sodium ion battery anode. *J. Alloys Compd.* **2020**, *825*, 154173. https://doi.org/10.1016/j.jallcom.2020.154173.
30. Yuan, B.; Luan, W.; Tu, S. One-step synthesis of cubic FeS_2 and flower-like $FeSe_2$ particles by a solvothermal reduction process. *Dalton Trans.* **2012**, *41*, 772–776. https://doi.org/10.1039/C1DT11176K.

31. Yue, C.; Zhang, X.; Yin, J.; Zhou, H.; Liu, K.; Liu, X. Highly efficient FeS_2@FeOOH core-shell water oxidation electrocatalyst formed by surface reconstruction of FeS_2 microspheres supported on Ni foam. *Appl. Catal. B-Environ.* **2023**, *339*, 123171. https://doi.org/10.1016/j.apcatb.2023.123171.
32. Sun, K.; Su, Z.; Yang, J.; Han, Z.; Liu, F.; Lai, Y.; Li, J.; Liu, Y. Fabrication of pyrite FeS_2 thin films by sulfurizing oxide precursor films deposited via successive ionic layer adsorption and reaction method. *Thin Solid Film.* **2013**, *542*, 123–128. https://doi.org/10.1016/j.tsf.2013.06.091.
33. Jiang, F.; Peckler, L.T.; Muscat, A.J. Phase Pure Pyrite FeS_2 Nanocubes Synthesized Using Oleylamine as Ligand, Solvent, and Reductant. *Cryst. Growth Des.* **2015**, *15*, 3565–3572. https://doi.org/10.1021/acs.cgd.5b00751.
34. White, S.N. Laser Raman spectroscopy as a technique for identification of seafloor hydrothermal and cold seep minerals. *Chem. Geol.* **2009**, *259*, 240–252. https://doi.org/10.1016/j.chemgeo.2008.11.008.
35. Sha, R.; Vishnu, N.; Badhulika, S.J.I.T. Single Step Synthesis of 2-D Marcasite FeS_2 Micro-Flowers Based Electrochemical Sensor for Simultaneous Detection of Four DNA Bases. *IEEE Trans. Nanotechnol.* **2022**, *21*, 374–379. https://doi.org/10.1109/TNANO.2022.3190223.
36. Liu, Y.; Jin, W.; Zhao, Y.; Zhang, G.; Zhang, W.J.A.C.B.E. Enhanced catalytic degradation of methylene blue by α-Fe_2O_3/graphene oxide via heterogeneous photo-Fenton reactions. *Appl. Catal. B: Environ.* **2017**, *206*, 642–652. https://doi.org/10.1016/j.apcatb.2017.01.075.
37. Liu, R.; Wang, Y.; Yang, Y.; Shen, L.; Zhang, B.; Dong, Z.; Gao, C.; Xing, B. New insights into adsorption mechanism of pristine and weathered polyamide microplastics towards hydrophilic organic compounds. *Environ. Pollut.* **2023**, *317*, 120818. https://doi.org/10.1016/j.envpol.2022.120818.
38. Wang, B.; Xu, Z.; Dong, B. Occurrence, fate, and ecological risk of antibiotics in wastewater treatment plants in China: A review. *J. Hazard. Mater.* **2024**, *469*, 133925. https://doi.org/10.1016/j.jhazmat.2024.133925.
39. Zou, Y.; Zhou, C.; Li, Z.; Han, X.; Tong, L.; Liu, T.; Xiong, L.; Bai, L.; Liang, J.; Fan, Y.; et al. Hydrophobic Tetracycline Immobilized in Fibrous Hyaluronan Regulates Adhesive Collagen-Based Hydrogel Stability for Infected Wound Healing. *Small* **2023**, *19*, 45. https://doi.org/10.1002/smll.202303414.
40. Dixon, P.; Chauhan, A. Effect of the surface layer on drug release from delefilcon-A (Dailies Total11®) contact lenses. *Int. J. Pharm.* **2017**, *529*, 89–101. https://doi.org/10.1016/j.ijpharm.2017.06.036.
41. Matilainen, A.; Gjessing, E.T.; Lahtinen, T.; Hed, L.; Bhatnagar, A.; Sillanpaa, M. An overview of the methods used in the characterisation of natural organic matter (NOM) in relation to drinking water treatment. *Chemosphere* **2011**, *83*, 1431–1442. https://doi.org/10.1016/j.chemosphere.2011.01.018.
42. Lin, K.-Y.A.; Lin, J.-T. Ferrocene-functionalized graphitic carbon nitride as an enhanced heterogeneous catalyst of Fenton reaction for degradation of Rhodamine B under visible light irradiation. *Chemosphere* **2017**, *182*, 54–64. https://doi.org/10.1016/j.chemosphere.2017.04.152.
43. Cheng, X.; Liang, L.; Ye, J.; Li, N.; Yan, B.; Chen, G. Influence and mechanism of water matrices on H_2O_2-based Fenton-like oxidation processes: A review. *Sci. Total Environ.* **2023**, *888*, 164814. https://doi.org/10.1016/j.scitotenv.2023.164086.
44. Zhang, B.-T.; Kuang, L.; Teng, Y.; Fan, M.; Ma, Y. Application of percarbonate and peroxymonocarbonate in decontamination technologies. *J. Environ. Sci.* **2021**, *105*, 100–115. https://doi.org/10.1016/j.jes.2020.12.031.
45. Yang, L.; Xiang, Y.; Jia, F.; Xia, L.; Gao, C.; Wu, X.; Peng, L.; Liu, J.; Song, S. Photo-thermal synergy for boosting photo-Fenton activity with rGO-$ZnFe_2O_4$.: Novel photo-activation process and mechanism toward environment remediation. *Appl. Catal. B-Environ.* **2021**, *292*, 120198. https://doi.org/10.1016/j.apcatb.2021.120198.
46. Wang, Y.; Chi, Z.; Chen, C.; Su, C.; Liu, D.; Liu, Y.; Duan, X.; Wang, S. Facet- and defect-dependent activity of perovskites in catalytic evolution of sulfate radicals. *Appl. Catal. B-Environ.* **2020**, *272*, 118972. https://doi.org/10.1016/j.apcatb.2020.118972.
47. Yu, H.; Liu, G.; Jin, R.; Zhou, J. Goethite-humic acid coprecipitate mediated Fenton-like degradation of sulfanilamide: The role of coprecipitated humic acid in accelerating Fe(III)/Fe(II) cycle and degradation efficiency. *J. Hazard. Mater.* **2021**, *403*, 124026. https://doi.org/10.1016/j.jhazmat.2020.124026.
48. Nie, Y.; Zhang, Y.; Nie, X.; Tian, X.; Dai, C.; Shi, J.J.J. Colloidal iron species driven enhanced H_2O_2 decomposition into hydroxyl radicals for efficient removal of methylene blue from water. *J. Hazard. Mater.* **2023**, *448*, 130949. https://doi.org/10.1016/j.jhazmat.2023.130949.
49. Huang, B.; Yang, C.; Zeng, H.; Zhou, L. Multivalent iron-based magnetic porous biochar from peach gum polysaccharide as a heterogeneous Fenton catalyst for degradation of dye pollutants. *Int. J. Biol. Macromol.* **2023**, *253*, 126753. https://doi.org/10.1016/j.ijbiomac.2023.126753.
50. Mei, S.-C.; Li, L.; Huang, G.-X.; Pan, X.-Q.; Yu, H.-Q. Heterogeneous Fenton water purification catalyzed by iron phosphide (FeP). *Water Res.* **2023**, *241*, 120151. https://doi.org/10.1016/j.watres.2023.120151.
51. Liu, J.; Zhang, Q.; Tian, X.; Hong, Y.; Nie, Y.; Su, N.; Jin, G.; Zhai, Z.; Fu, C.J.C.E.J. Highly efficient photocatalytic degradation of oil pollutants by oxygen deficient SnO_2 quantum dots for water remediation. *Chem. Eng. J.* **2021**, *404*,

127146. https://doi.org/10.1016/j.cej.2020.127146.

52. Jin, Z.; Li, Q.; Tang, P.; Li, G.; Liu, L.; Chen, D.; Wu, J.; Chai, Z.; Huang, G.; Chen, X.J.N.A. Copper-doped carbon dots with enhanced Fenton reaction activity for rhodamine B degradation. *Nanoscale Adv.* **2022**, *4*, 3073–3082. https://doi.org/10.1039/d2na00269h.
53. Yang, X.; Zhang, X.; Wang, Z.; Li, S.; Zhao, J.; Liang, G.; Xie, X. Mechanistic insights into removal of norfloxacin from water using different natural iron ore-biochar composites: More rich free radicals derived from natural pyrite-biochar composites than hematite-biochar composites. *Appl. Catal. B-Environ.* **2019**, *255*, 117752. https://doi.org/10.1016/j.apcatb.2019.117752.
54. Nesbitt, H.; Scaini, M.; Hochst, H.; Bancroft, G.; Schaufuss, A.; Szargan, R.J.A.M. Synchrotron XPS evidence for Fe^{2+}-S and Fe^{3+}-S surface species on pyrite fracture-surfaces, and their 3D electronic states. *Am. Mineral.* **2000**, *85*, 850–857. https://doi.org/10.2138/am-2000-5-628.
55. Lu, Z.; Wang, N.; Zhang, Y.; Xue, P.; Guo, M.; Tang, B.; Bai, Z.; Dou, S. Pyrite FeS_2@C nanorods as smart cathode for sodium ion battery with ultra-long lifespan and notable rate performance from tunable pseudocapacitance. *Electrochim. Acta* **2018**, *260*, 755–761. https://doi.org/10.1016/j.electacta.2017.12.031.
56. Chen, J.; Zhou, X.; Mei, C.; Xu, J.; Zhou, S.; Wong, C.-P. Pyrite FeS_2 nanobelts as high-performance anode material for aqueous pseudocapacitor. *Electrochim. Acta* **2016**, *222*, 172–176. https://doi.org/10.1016/j.electacta.2016.10.181.
57. Ye, Z.; Padilla, J.A.; Xuriguera, E.; Beltran, J.L.; Alcaide, F.; Brillas, E.; Sires, I. A Highly Stable Metal-Organic Framework-Engineered FeS_2/C Nanocatalyst for Heterogeneous Electro-Fenton Treatment: Validation in Wastewater at Mild pH. *Environ. Sci. Technol.* **2020**, *54*, 4664–4674. https://doi.org/10.1021/acs.est.9b07604.
58. Morales-Gallardo, M.V.; Ayala, A.M.; Pal, M.; Cortes Jacome, M.A.; Toledo Antonio, J.A.; Mathews, N.R. Synthesis of pyrite FeS_2 nanorods by simple hydrothermal method and its photocatalytic activity. *Chem. Phys. Lett.* **2016**, *660*, 93–98. https://doi.org/10.1016/j.cplett.2016.07.046.
59. Zhang, Q.; Li, Y.; Li, H.; Zhang, Y.; Zhang, L.; Zhong, S.; Shu, X. Multi-catalysis of glow discharge plasma coupled with FeS_2 for synergistic removal of antibiotic. *Chemosphere* **2023**, *312*, 137204. https://doi.org/10.1016/j.chemosphere.2022.137204.
60. Ma, C.; Liu, Y.; Wang, J.; Evrard Deric, N.T.; Li, Y.; Fan, X.; Peng, W. Facile synthesis of pyrite FeS2 on carbon spheres for high-efficiency Fenton-like reaction. *Chemosphere* **2024**, *355*, 141799–141799. https://doi.org/10.1016/j.chemosphere.2024.141799.
61. Zhu, L.; Wang, H.; Sun, J.; Lu, L.; Li, S. Sulfur Vacancies in Pyrite Trigger the Path to Nonradical Singlet Oxygen and Spontaneous Sulfamethoxazole Degradation: Unveiling the Hidden Potential in Sediments. *Environ. Sci. Technol.* **2024**, *58*, 6753–6762. https://doi.org/10.1021/acs.est.3c09316.
62. Chen, X.; Hu, T.; Zhang, J.; Yang, C.; Dai, K.; Pan, C.; Compounds, Diethylenetriamine synergistic boosting photocatalytic performance with porous g-C_3N_4/CdS-diethylenetriamine 2D/2D S-scheme heterojunction. *J. Alloys Compd.* **2021**, *863*, 158068. https://doi.org/10.1016/j.jallcom.2020.158068.
63. Zhang, W.; Chen, Y. Experimental determination of conduction and valence bands of semiconductor nanoparticles using Kelvin probe force microscopy. *J. Nanoparticle Res.* **2013**, *15*, 1–7. https://doi.org/10.1007/s11051-012-1334-2.